TITLE:

MICROMANIPULATION OF LIVE MICRODISSECTED TISSUES WITH A LOW-COST INTEGRATED ROBOTIC PLATFORM

Noah R. Gottshall,*#[1] Ivan Stepanov,*[1,3] Alireza Ahmadianyazdi,[1] Daksh Sinha,[3] Ethan Lockhart,[1] Tran N. Nguyen,[1] Sarmad Hassan,[3] Lisa Horowitz,[1] Ray Yeung,[2] Taranjit S. Gujral,[4] Albert Folch[1]

* Equal contribution

Email: noahgottshall@gmail.com

[1] Department of Bioengineering, University of Washington, Seattle, WA, USA.

[2] Department of Surgery, University of Washington, Seattle, WA, USA.

[3] Department of Mechanical Engineering, University of Washington, Seattle, WA, USA.

[4] Human Biology Division, Fred Hutchinson Cancer Center, Seattle, WA, USA.

ABSTRACT

The small amount of human tissue available for testing is a paramount challenge in cancer drug development, cancer disease models, and personalized oncology. Technologies that combine the microscale manipulation of tissues with fluid handling offer the exciting possibility of miniaturizing and automating drug evaluation workflows. This approach minimizes animal testing and enables inexpensive, more efficient testing of samples with high clinical biomimicry using scarce materials. We have developed an inexpensive platform based on an off-the-shelf robot that can manipulate microdissected tissues (µDTs) into user-programmed positions without using intricate microfluidic designs nor any other accessories such as a microscope or a pneumatic controller. The robot integrates complex functions such as vision and fluid actuation by incorporating simple items including a USB camera and a rotary pump. Through the robot's camera, the platform software optically recognizes randomly-seeded µDTs on the surface of a petri dish and positions a mechanical arm above the µDTs. Then, a custom rotary pump actuated by one of the robot's motors generates enough microfluidic lift to hydrodynamically pick and place µDTs with a pipette at a safe distance from the substrate without requiring a proximity sensor. The platform's simple, integrated construction is cost-effective and compact, allowing placement inside a tissue culture hood for sterile workflows. The platform enables users to select µDTs based on their size, place them in user-programmed arrays, such as multi-well plates, and control various robot motion parameters. As a case application, we use the robotic system to conduct semi-automated drug testing of mouse and human µDTs in 384-well plates. Our user-friendly platform promises to democratize microscale tissue research to clinical and biological laboratories worldwide.

INTRODUCTION

There has been a fast-rising interest in miniaturizing the process of drug development via the production of submillimeter-sized 3D tissues ("microtissues"), either by bottom-up approaches (*i.e.*, bioprinting,[1] microengineering,[2,3] or aggregation from single cells[4–6] to build organs-on-chips or organoids) or, conversely, top-down microdissection from biopsies (*i.e.*, µDTs, encompassing organospheres, spheroids, tumoroids, etc.).[7–14] Microtissues are increasingly used for disease modeling in cancer[15] and immunology,[16] as well as for regenerative medicine,[17] personalized medicine,[18–20] and drug screening.[18,21] Because of their small size, the high-throughput manipulation and culture of microtissues has spurred the development of high-precision microfluidic tools such as hanging drops,[22,23] droplet microfluidics,[20] and/or microfluidic perfusion.[6,10,24–27] While these tools ensure the fluidic compartmentalization and microenvironmental control of the microtissues, they entail complex fluid control systems that are not plug-and-play, requiring human experts for their fabrication and operation, which can severely limit the translation of microtissues to the clinic.

Various robotic platforms address the lack of user-friendliness of microfluidic platforms by automating the handling (*i.e.*, pipetting and transferring) of microtissues. However, present robotic manipulators require a microscope, a pneumatic controller, or both,[28] and existing commercial systems are bulky, expensive robots with integrated air handling for sterility. To broaden access to microtissue research, we have developed a user-friendly, cost-effective robotic platform (**Fig. 1**). Our system operates without the need fora microscope or a pneumatic system and the compact size allows seamless integration into a standard tissue culture hood (see **Suppl. Fig. 1**). Compared to the existing commercial robotic dispenser systems (see competitor comparison in Suppl. Mater.), our system features three key advantages: i) Our platform does not require a microscope but instead uses a high-resolution USB camera (**Fig. 1**A) to help sort and pick live µDTs. The µDTs are typically picked sequentially from a random distribution of µDTs (*e.g.*, in a petri dish) and then placed into a multi-well plate by means of an off-the-shelf robot for pick-and-place applications (**Fig. 1**B). ii) Our platform builds on an inexpensive, compact 4-axis articulated-arm robot, a design which enables sterile workflows within modest

budgets. iii) Our platform integrates a custom CNC-milled rotary pump powered by the end-effector ("head") motor of the robotic arm (**Fig. 1**B inset and Rotary Pump in Suppl. Mater.). This integrated solution simplifies and substantially lowers the cost of programmable fluid manipulation. The same Python interface that controls the translational motors also programs the pump actions needed to pick and place μDTs via flow, bypassing the need for a separate pneumatic or syringe pump controller.

To demonstrate the utility of our platform, we present robotic manipulations of both mouse and human μDTs (average 250 or 400 μm-wide) mechanically–cut with a tissue chopper (see Methods). We term these tissues "cuboids"[24] because they result from three orthogonal cuts, resulting in a cuboidal shape at day 0. While human cuboids retain their cuboidal shape and mouse cuboids relax to a spheroid shape after a few days in culture for both sizes, for simplicity we call them "cuboids" regardless of their shape (and species). Here we show that the technology applies equally well for manipulating the tested microtissue shapes, sizes, and species. We also demonstrate robotic protocols to pick single cuboids, place and sort them in separate wells according to their size, sort hundreds of microtissues in less than one hour, and perform drug evaluations of patient biopsies with multiple drugs on 384-well plates to simulate realistic drug evaluations of potential clinical utility.

RESULTS AND DISCUSSION

Parameters for cuboid picking

We first evaluated the parameters that affect cuboid picking by our robotic platforms. We confirmed that the nominal resolution of the robot (50 μm) provided by the manufacturer is sufficient for picking up cuboids. Using high-resolution video, we measured the accuracy and precision of the localization of cuboids by the robotic platform. The accuracy, or the distance between the center of the pipette and the intended target (the center of the cuboid), was measured at 129 ± 23 μm (**Fig. 2**A, Suppl**. Video 1)**. The precision, or the repeatability of localization, was measured at 26 ± 3 μm. A user starts the platform's operation by calibrating the camera coordinate system with the robot's coordinate system, so that the camera "learns" about the physical dimensions of the workplace. Calibration is an automated process based on the reflections of a laser mounted on the head of the robot (see Calibration in Suppl. Mater.). Next, the user places a random distribution of cuboids in the petri dish and uses the software to take a picture of the petri dish. The software automatically registers the coordinates of each cuboid's projected (2D) center of mass. These coordinates are used to direct the pipette atop the cuboids. Before starting, the user is prompted to specify which range of cuboid sizes will be picked (see Size Selection in Suppl. Mater.).

Live cuboids are picked from the surface of the petri dish using a microfluidic lift-off process (**Fig. 2**B-E) powered by a custom-made rotary pump. We fabricated the pump by CNC-milling PMMA (see Methods) and installed it right below the robot's head so that the head's motor is aligned with and powers the rotary pump (**Suppl. Fig. 1**B&C). We used a rollerless eccentric rotary pump design to avoid pulsatility. The rotary pump coupled to the robot's head can thus be easily programmed via Python. The pump can rotate 360 degrees (or a fraction thereof) in either direction resulting in a range of pumping rates of 0 – 139.8 μL/s (**Suppl. Video 2**). The pump, connected to a glass pipette (0.936 mm ID and 1.372 mm OD), can generate the (backward) lift flow Q that is needed to pick a cuboid off a surface (~5 μL, $Q =$ 380 μL/s), stop the flow to keep the cuboid inside the pipette during the translation of the arm, and generate the (forward) flow to dispense the cuboid at the target location. **Fig. 2**B shows a sequence of four photographs depicting the process of pipette approach, the point when the pipette is at a closest distance, cuboid lift off and suction into the pipette (Suppl**. Video 3**).

A theoretical fluidic analysis illustrates why lifting a cuboid does not require high-precision instrumentation (*e.g.*, a microscope or, in its default, a proximity sensor) to position the pipette in z near the surface. The pipette mounted at the head of the robot provides suction flow (**Fig. 2**C) that we can model as a point sink (**Fig. 2**D). For a cuboid of volume V_c and density ρ_c, its weight is $W = \rho_c V_c g$ and the buoyant force it experiences is $F_B = \rho V_c g$ where ρ is the density of the fluid (water). Hence the following inequality must be satisfied:

$$\left(\bar{p}_{bottom} - \bar{p}_{top}\right) A \geq W_g - F_B \quad \textbf{(Eqn. 1)}$$

where $\bar{p}_{bottom}$ and $\bar{p}_{top}$ are the average fluid pressures at the bottom and top surfaces of the cuboid, respectively, and A ~ (400 μm)^2 is the area of one of the faces of the cuboid. Applying Bernouilli's equation, $\bar{p}_{bottom} = \rho g h$ and $\bar{p}_{top} = \rho g h - 1/2 \rho v^2$, where v is the average flow velocity on top of the cuboid, **Eqn. 1** can be re-written as:

$$v \geq \sqrt{\frac{2(\rho_c - \rho)V_c g}{\rho A}} \quad \textbf{(Eqn. 2)}$$

Since v has components u_x, u_y, and u_z, where u_y and $u_z \ll u_x$ because the pipette is centered with the cuboid, then $v \approx u_x$, where u_x can be obtained from ideal flow equations through the method of images:[29]

$$u_x = \frac{Q(x-d)}{\left[(x-d)^2 + y^2 + z^2\right]^{3/2}} + \frac{Q(x+d)}{\left[(x+d)^2 + y^2 + z^2\right]^{3/2}} \quad \textbf{(Eqn. 3)}$$

In **Eqn. 3**, Q is the suction flow rate generated by the pump, d is the distance between the cuboid's bottom surface and the suction pump, and x, y, and z refer to the distances from the coordinate system located at the cuboid. Thus, we can find the flow velocity on top of the cuboid by substituting $x = h$ into **Eqn. 3**. Assuming $h \ll d$, we obtain $v = 2Qh/d^3$. Substituting into **Eqn. 2**, we obtain a condition for cuboid lifting to occur:

$$d \leq d_{max} = \left[\frac{2Q^2h^2\rho A}{(\rho_c - \rho)V_c g}\right]^{1/6}$$

where $h \approx$ 400 μm. Note that d_{max} is not very sensitive to changes in any of the parameters. Since $A \approx h^2$ and $V_c \approx h^3$, then $d_{max} \sim h^{1/6}$. Substituting typical values ($Q =$ 380 μL/s), we find that the maximum distance between the pipette and the bottom of a cuboid that allows for lifting the cuboid is $d_{max} \approx$ 1.2 mm for a 400 μm cuboid and $d_{max} \approx$ 1.1 mm for a 250 μm cuboid.

Measurements of cuboid picking success as a function of *z* (**Fig. 2**E) validate this analysis: the pipette needs to be at most ~1.3 mm above the surface to lift a 400 μm cuboid, which is in close agreement with our point-sink model. We have observed that cuboids can be lifted with much smaller Q values, even with the capillary flow that spontaneously ascends into the pipette, but larger values have the benefit of speeding up the process. The "lift" effect happens for a wide substrate-to-pipette distance range of 0.4-1.3 mm (0-900 μm above a 400 μm cuboid), which bypasses the need for a proximity sensor.

A major advantage of the robotic platform over previous microfluidic-based microtissue manipulation platforms is that it can straightforwardly incorporate software-based checks and diagnostics that minimize and quantify error rates. To eliminate the possibility that the pipette lifts two or more adjacent cuboids, we measured the sensitivity of the pipette to picking nearby cuboids unintendedly. Thus, we measured the success of cuboid picking as a function of *r*, the lateral distance between the center of the cuboid and the center of the pipette, for many values of *z* (**Fig. 2**E). The transfer success plot displays an interesting "mushroom" profile: right above the cuboid (within 0.4 mm, or its own height), the pipette only lifts the cuboid when its center is within the margins of the cuboid. However, at heights larger than 0.4 mm above the cuboid, the lift radius L_R increases suddenly from L_R = 0.2 mm to L_R = 1.2 mm from the center of the cuboid (**Fig. 2**E). At the usual *z* = 0.8 mm where we place the pipette, the success decays rapidly to 0% for *r* > 1.4 mm. This mushroom profile has an immediate consequence on the ability to discriminate between two adjacent cuboids: the user can either choose to hover at low pipette-to-substrate *z* heights (risking crashing of the pipette) for high selectivity or hover at higher *z* (thus losing the ability to discriminate between two adjacent cuboids) for higher safety. We decided for safety because not all petri dishes are equally planar and it is straightforward to use image recognition methods to select for properly-distanced cuboids. Hence, for safety, we operate at *z* = 0.8 mm and pick only cuboids that are at least 2 mm away from another cuboid (see Transfer Success in Suppl. Mater., **Suppl. Fig. 2**).

We obtained statistics on the success rates of cuboid transfer by the robotic platform, with success being defined as a well filled with a single cuboid. We observed that 94.2 ± 1.8% of the transfer attempts were successful, 3.06 ± 1.07% were failures (the well was empty) and in 2.74 ± 0.75% of the cases two cuboids were transferred instead of one (statistics based on filling six 384-well plates with tissue samples from different batches; two well plates were filled with PY8119 mouse tumors, and four well plates were filled with two colorectal cancer human tissue tumors). This small amount of failure rates does not pose a problem for drug test analysis, as the failures can be discarded during imaging.

Since cuboid size can be a confounder in studies of cytokine secretion (the number of cells affects the readout) and hypoxia-induced cell death, we implemented a size-sorting software feature that allows for picking narrow

cuboid size ranges and deliver them to pre-programmed areas of the multi-well plate (**Fig. 3**). The experiment validates that the setup is not restricted to 400 μm-wide cuboids, as it can also enable other applications necessitating the manipulation of much smaller and larger microtissues simply by changing the size threshold in the software. Importantly, the controls show that robotic manipulation does not affect tissue viability (see Suppl. Mater. and **Suppl. Fig. 7**). Mouse tumor cuboids sorted by the robot of two different sizes (250 and 400 μm) had virtually the same death rate responses when exposed to various cytotoxic agents (**Fig. 4**A&B), showing that the robot can be used to implement very benign sorting schemes. However, articulated robots have complex kinematics, so they are not very fast. It is likely that similar pick-and-place operations could be achieved in less time with gantry-type robots which are less complex and faster (but less cost-effective).

Robotic loading facilitates straightforward drug evaluations in multi-well plates with fluorescent readouts of various types and sizes (**Fig. 4**). A size-selection procedure was executed on the platform to distinguish and select between 250 μm and 400 μm cuboids from a mixed sample. A 96 well-plate was divided into two sections for the two sizes (**Fig. 4A**). The 96-well plate was filled in ~15 min. Equal drug combinations were applied to each half of the plate, with cisplatin (CP, an alkylating chemotherapeutic) versus medium control, and staurosporine (STS, a non-specific kinase inhibitor used as a positive control for cell death), versus DMSO vehicle control. Cell death was measured after treatment for 3 days by the mean fluorescent intensity of Sytox Green (SG), a green nuclear cell death indicator. Analysis revealed near equal trends of the drug additions between both cuboid sizes (**Fig. 4B**).

We performed similar experiments on a different tumor, with U87 glioma mouse xenograft tumor cuboids, and with a more extensive drug panel (**Fig. 4**C-F). After loading 400 μm cuboids onto a 96 well plate, we exposed the cuboids to the indicated drugs for 3 days. After staining with the blue nuclear stain Hoechst, and the dead nuclear stain SG, we saw clear drug effects. The graph shown in **Fig. 4**D displays the significant differences among the average fluorescent readout values of several drug conditions as indicated by the asterisks above.

The robotic platform also served to extend the throughput of drug testing, by filling multiple plates consecutively and increasing the plate size to 384-well plates. The ~1.3 mm OD glass micropipette end-effector allows full range of clearance through 96 and 384 well plate wells. Simple user input allows for the interchange of the two plate variations and the suction-deposit volume. **Fig. 5** shows the results of a proof-of-concept two-drug evaluation after 3 days treatment of Py8119 mouse breast tumor cuboids with CP and STS at five different logarithmic concentrations. The use of 384-well plates allowed for ~32 cuboids per drug condition, demonstrating the ability of the robot to handle large sample sizes efficiently. In this experiment, the plate was filled in only ~65 min and the success rate of wells filled with one cuboid was 98% (378/384). The SG cell death fluorescent readouts for each condition represent statistically significant results when compared to control cuboids, with a linearly increasing cell-death trend for the increasing STS concentrations.

We next used the robotic platform to perform a drug evaluation on cuboids from a patient colorectal cancer (CRC) liver metastasis conducted with clinically relevant drugs. The patient was a 54-year-old male with recurrent CRC after previous surgery and chemotherapy including FOLFOX. We took three core biopsies and prepared cuboids from 6 slices for each of the three cores (**Fig. 6**A). Using the robot, we filled the wells of a 384-well plate with individual cuboids, with one plate for each of the three cores. Across the three 384-well plates, the filling of 1,046 wells was attempted, with 953 wells filled with single cuboids, 41 wells filled with double cuboids and 52 wells were failures (overall success rate 0.91%). After overnight culture with RealTime-Glo (RTG), we measured the baseline viability as luminescence with an IVIS machine (**Fig. 6**B). There was much more variability in the baseline viability between cuboids, as may be expected from a heterogenous patient tumor, especially since some of the tumor areas appear to correspond to areas with post-necrotic changes. Furthermore, core 1 displayed the most viability out of the three cores, followed by core 3 and then core 2. Next, the following combination drugs were applied for each core: FOLFOX (5-fluorouracil (5-FU) 1 μg/mL / oxaliplatin 1 μg/mL) and gemcitabine (GC)/cisplatin (GC 1 μM, CP 5 μM) are standard cytotoxic chemotherapies. Regorafenib (Re, 0.5 μM) and Fruiquintinib (Fr, 0.5 μM) are targeted kinase inhibitors used for CRC. STS was used at 1 μM as a positive control. DMSO vehicle controls (0.2% for cytotoxic drugs, 0.05% for kinase inhibitors) as well as a medium alone served as negative controls. We measured viability by RTG after 4 days and after 6 days with similar results for both (**Fig. 6**B). Drug responses display very similar results across all 3 cores, with STS having the only statistically significant response (**Fig. 6**C), which is not unexpected given the patient's prior exposure to the chemotherapy drugs.

Crucially, the platform is agnostic to the type of tissue (shape or species) being used. Therefore, the platform could easily be extended to other human tumor microtissues (organoids, etc.) to allow for tests that are relevant to the human tumor microenvironment (TME) and to inform drug testing modalities such as immunotherapy that require the preservation of the TME *in vitro*. The number of clinical trials of combination therapies has been climbing at an unsustainable rate: 3,362 trials have been launched since 2006 to test PD-1/PD-L1-targeted monoclonal antibodies alone or in combination with other agents, with a ~200% increase in

active trials just from 2017 to 2019.[30] Given the nearly infinite number of potential combinations and the limited resources to test them, the inexpensive, TME-friendly *ex vivo* testing platform demonstrated here could enable a distributed approach to drug testing where large numbers of clinical laboratories collaborate to identify the most suitable drug candidates for clinical trials.

CONCLUSIONS

Our data collectively shows that our user-friendly robotic platform allows untrained biomedical researchers to conduct low-cost drug evaluations with live microtissues. The platform is agnostic to tissue size (250 µm and 400 µm), shape (cuboidal and spheroid), and species (mouse and human). Starting with a small amount of tumor tissue, the platform can reliably gather a large amount of functional information such as drug efficacy data from fluorescence readouts in standard multi-well plates by sorting hundreds of microtissues in less than one hour. Compared to traditional pipette dispensers, our compact robot is very cost-effective and achieves monodisperse distributions of cuboids, which could prove essential for measuring the effect of tumor heterogeneity in drug responses as well as in assays where the cuboid's functional response can be influenced by the concentration of secreted molecules, *e.g.*, in cytokine secretion assays.

METHODS

Fabrication and operation of the rotary pump:

The pump utilizes ring bearing design to generate peristalsis along a 1.3 ID silicone tube. PMMA of 8 mm thickness was cut with a CNC mill for the pump housing. A 3D printed central axle holds 3 metal ball bearings of varying sizes. Two identical flanged bearings hold the central axle in place and allow for low friction and controlled movements. A third bearing is mounted in the middle, eccentrically to the inner PMMA casing. Four aluminum screws of 3 mm diameter lock the pump to the stepper motor attached as the end-effector on the robotic arm. Tube replacement can be easily achieved by removing the screws and opening the housing. Peristalsis occurs as the eccentric ring bearing rolls around the silicone tube, pressed against the inner housing. The peristaltic movement generates fluid displacement in the tube, causing fluid to be suctioned upwards into the pipette attached to the silicone tube, or dispensed downward out of the pipette, depending on the direction of rotation of the motor (See Suppl. Mater. Rotary pump section for more details).

Cell culture:

The Py8119 syngeneic mouse breast adenocarcinoma cell line (American Type Culture Collection (ATCC), CRL 3278) and U87-MG (ATCC) were grown in DMEM/F12 supplemented with 5% FBS and 1% penicillin/streptomycin. Tissue culture reagents were obtained from GIBCO, ATCC, or Fisher.

Tumor generation for mouse model:

Mice were handled in accordance with institutional guidelines and under protocols approved by the Animal Care and Use Committee at the University of Washington, Seattle and by the Fred Hutchinson Cancer Research Center. For the Py8119 mouse syngeneic tumors, we injected 1-2 x 10^6 cells in Matrigel (Corning) orthotopically into the mammary fat pad of > 6 week-old female C57BL mice (Jackson Laboratories). For U87-MG human glioma cells xenograft tumors, we injected 1-2 x 10^6 cells subcutaneously in 6-8 week-old male athymic nude mice (Jackson Laboratories). Tumors were harvested at < 2 cm^3. If not used immediately, the tumor was stored up to overnight in Belzer-UW cold storage medium (Bridge-to-Life Ltd).

Human tissue:

Human tissue was obtained with written informed consent and treated in accordance with Institutional Review Board approved protocols at the University of Washington, Seattle. The biopsy was from a 54 year-old male with recurrent colorectal cancer metastatic to the liver and peritoneum. He had previously received surgery, treatment with IR liver ablation, and chemotherapy with CP, irinotecan, leucovorin and 5-FU.

Cuboid generation and culture:

We generated cuboids as previously described.[24] We embedded tissue punches (600 µm diameter, Harris Uni-Core) in 1-2% lomelt agarose and then cut slices using a Leica VT 1200 S vibrating microtome or MZ5100 vibratome (Lafayette Instruments). We cut the slices into cuboids with a tissue chopper (McIlwain tissue chopper (Ted Pella, Inc.), then gently dissociated the cuboids with a transfer pipette. For 400 µm cuboids, we filtered them for size less than the 750 µm filter and greater than a 300 µm filter (Pluriselect). Tissue was

handled using ice-cold DMEM/F12. After transfer of the cuboids to a 100 μm cell strainer (Corning or Falcon), we washed them twice with sterile PBS and once with medium. For the human CRC tumor, we did these washes in sterile tubes instead. For the CRC cuboids, the culture medium was Williams' Media E (Sigma) supplemented with nicotinamide (12 mM), L- ascorbic acid 2-phosphate (50 mg/mL), D-(+)-glucose (5 mg/mL) from Sigma; sodium bicarbonate (2.5%), HEPES (20 mM), sodium pyruvate (1 mM), Glutamax (1%), and penicillin–streptomycin (0.4%) from Gibco; and ITS + Premix (1%) and human EGF (20 ng/mL) from BD Biosciences. For the mouse cuboid experiments the culture medium was DMEM/F12 with 5% heat-inactivated fetal bovine serum, penicillin-streptomycin (0.1%).

Drug treatment and imaging:

To measure viability, RealTime-Glo (Promega) was added at 1x or 0.5x and the baseline luminescence was read the following day by IVIS (Perkin-Elmer). Drug was added to the well, and luminescence was read again after incubation with drug without further addition of RealTime-Glo. To measure cell death as an endpoint, SYTOX Green (1/50,000; Invitrogen), and/or Hoechst (16 μM, Invitrogen) were added to the well, incubated for 1 hr at 37°C, then imaged with or without washing twice in PBS. We took images using a Canon DS126601 on a Nikon SMZ1000 dissecting scope and a BZ-X800 (Keyence) microscope.

Robotic platform setup:

To become operational, the robotic platform needs to go through a physical setup process (platform assembly and pipette alignment) and a calibration between the camera and the robotic arm. The robotic arm is outfitted with a laser pointer for calibration (used as a reference point), the custom rotary pump connected to a capillary pipette, and a custom workspace platform for housing the culture dishes and well plates. A camera is positioned with a holder above the microtissue-containing culture dish. To increase the contrast (cuboids are opaque), the petri dish is back-illuminated by a flat white LED panel at all times. All devices that require power are plugged into a wall socket; the camera and robotic arm are connected to a PC with respective cables for data transfer. After the physical setup, a mapping between the robot's and the camera's system of coordinates needs to be established. The mapping is established with the assistance of a special calibration dish that is placed in the field of view of the camera. The robotic arm moves through the predefined positions located on the calibration dish, while the camera records the position of the laser dot in the calibration dish. Once the positions have been recorded, a coordinate transformation matrix can be calculated, finishing the calibration process (see Camera to robot calibration in Suppl. Mater.). Using a special pipette alignment dish, the pipette is aligned to the reference point of the robotic arm (see Pipette Alignment in Suppl. Mater.). The robotic platform is then ready for operation.

Programming of the automatic tissue transfer procedure:

The user is required to initialize several input variables that affect the automatic tissue transfer procedure. These variables include the picking size range, minimum distance to nearest neighbor, indexes of the wells to fill (in other words, how many cuboids to transfer), etc. The target type (a 96- or 384-well plate or a custom location or locations) should also be chosen. The transfer procedure can then be started: Images taken by the camera are analyzed by the software and information on the location of the microtissues is given to the robot. The software analyzes the distribution of the tissue samples and filters out those that do not fit the preset conditions. Activating the rotary pump, the robotic arm suctions ~5 μL of fluid, which lifts an automatically selected tissue sample and deposits it at the target location by returning the same volume. If the tissue samples that are left in the culture dish do not satisfy picking conditions, the process auto-pauses so their distribution can be reset by the user manually shaking the culture dish. The robotic arm then continues the transfer procedure until either the target number of tissues is fulfilled, or the distribution needs to be reset again. The software can determine failed transfer attempts, rectifying them by refilling wells that were left empty unintentionally. Using this straightforward protocol, our robotic platform can fill a 384-well plate in ~40 min.

AUTHOR CONTRIBUTIONS

Students Ivan Stepanov and Noah Gottshall designed the pump, the robot's procedures, and the Python code to control the robot, and conducted all the robotic and wet-lab experiments in this work. Daksh Sinha, Sarmad Hassan and Ivan Stepanov developed the GUI. Alireza Ahmadianyazdi developed the fluid dynamics model of cuboid picking. Ethan Lockhart CNC-milled the plastic pump and platform components. Lisa Horowitz, Tran Nguyen, and Ethan Lockhart prepared mouse tissues and cuboids. Ivan Stepanov, Noah Gottshall, Lisa Horowitz, and Albert Folch designed experiments and wrote the paper.

ACKNOWLEDGMENTS

This project was partially funded by the National Cancer Institute grants R21CA269097, 2R01CA181445, and R01CA272677. We thank Heidi Kenerson for preparing the human tumor tissue slices.

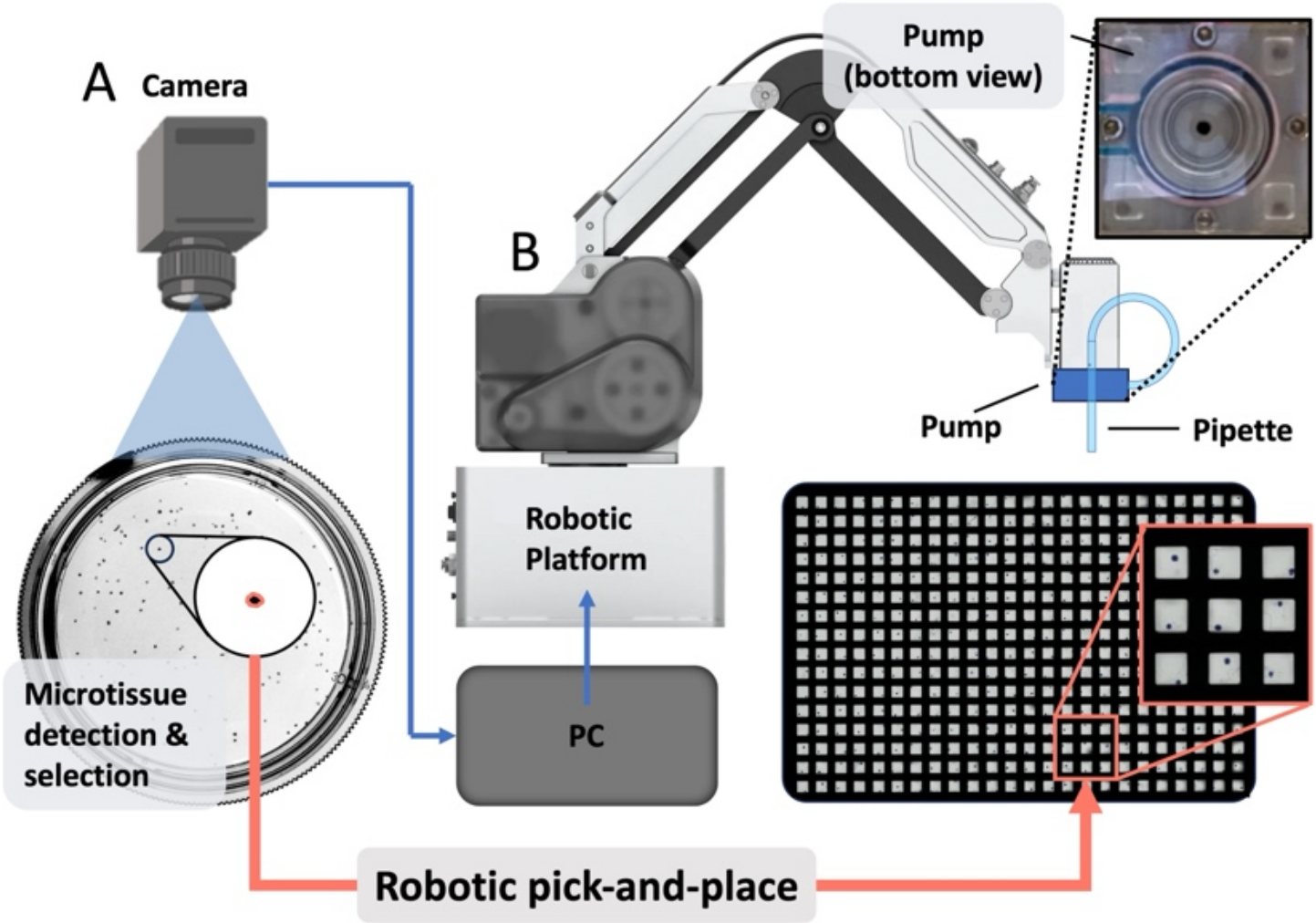

Figure 1. Robotic platform for automated pick-and-place of microtissues from a petri dish to a multi-well plate. (A) Schematic of the setup depicting the petri dish, a random distribution of microtissues, and the camera above. **(B)** Conceptual rendering of the robot's operation depicting the image that guides the robot's movements, the robot assembled with the pump, and the pipette at its head above a 384-well plate (inset: 3 × 3 array of wells containing 400 µm cuboids). The microtissue distribution is analyzed by a PC using images taken by the camera. The software selects a suitable tissue sample to be transferred to the target well plate by the robotic platform. Activating the pump, the robot suctions the tissue sample into the pipette and transfers it to the target well. Top inset: Bottom view of the rotary pump.

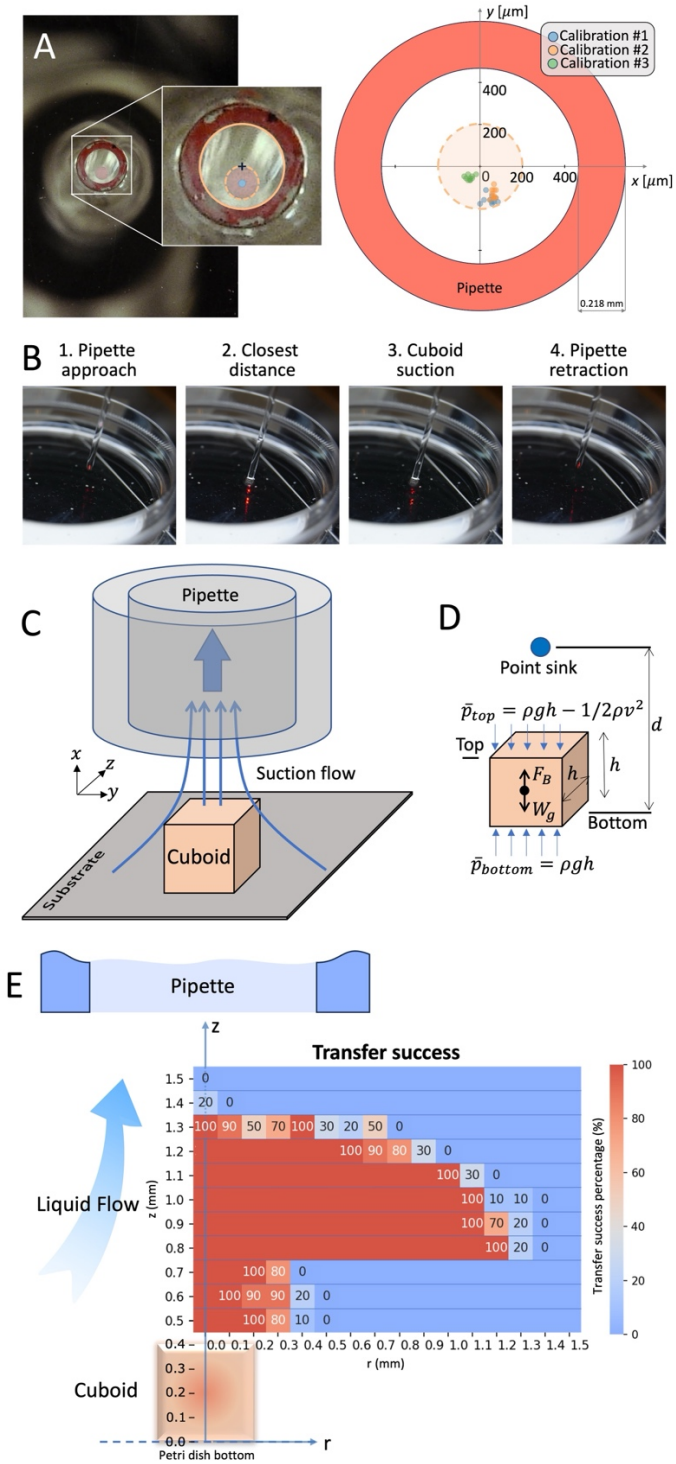

Figure 2. Microfluidic 'lifting' of a cuboid using a robotic-controlled pipette and flow. (A). (Left) Micrograph of a spherical cuboid (highlighted in blue) after the pipette's approach, with the pipette clearly visible as a red-painted rim. The photo was taken from underneath the petri dish. (Right) Graph depicting, for three different calibrations, the actual position of the center of the pipette with respect to the center of the cuboid, at (0,0), after the pipette was instructed to target (0,0). **(B)** Sequence of photographs depicting the process of cuboid picking from a surface. **(C)** Schematic setup with the pipette above the cuboid and **(D)** the approximation of the pipette as a point sink. Since the necessary distance required to lift a cuboid off a surface is predicted to be $d \leq$ 1.2 mm for a 400 μm cuboid, the procedure is compatible with a low-cost robotic setup. **(E)** Graph depicting the success of cuboid picking as a function of radial distance from the cuboid's position and the height of the pipette above the petri dish bottom, with schematic of cuboid and pipette to scale.

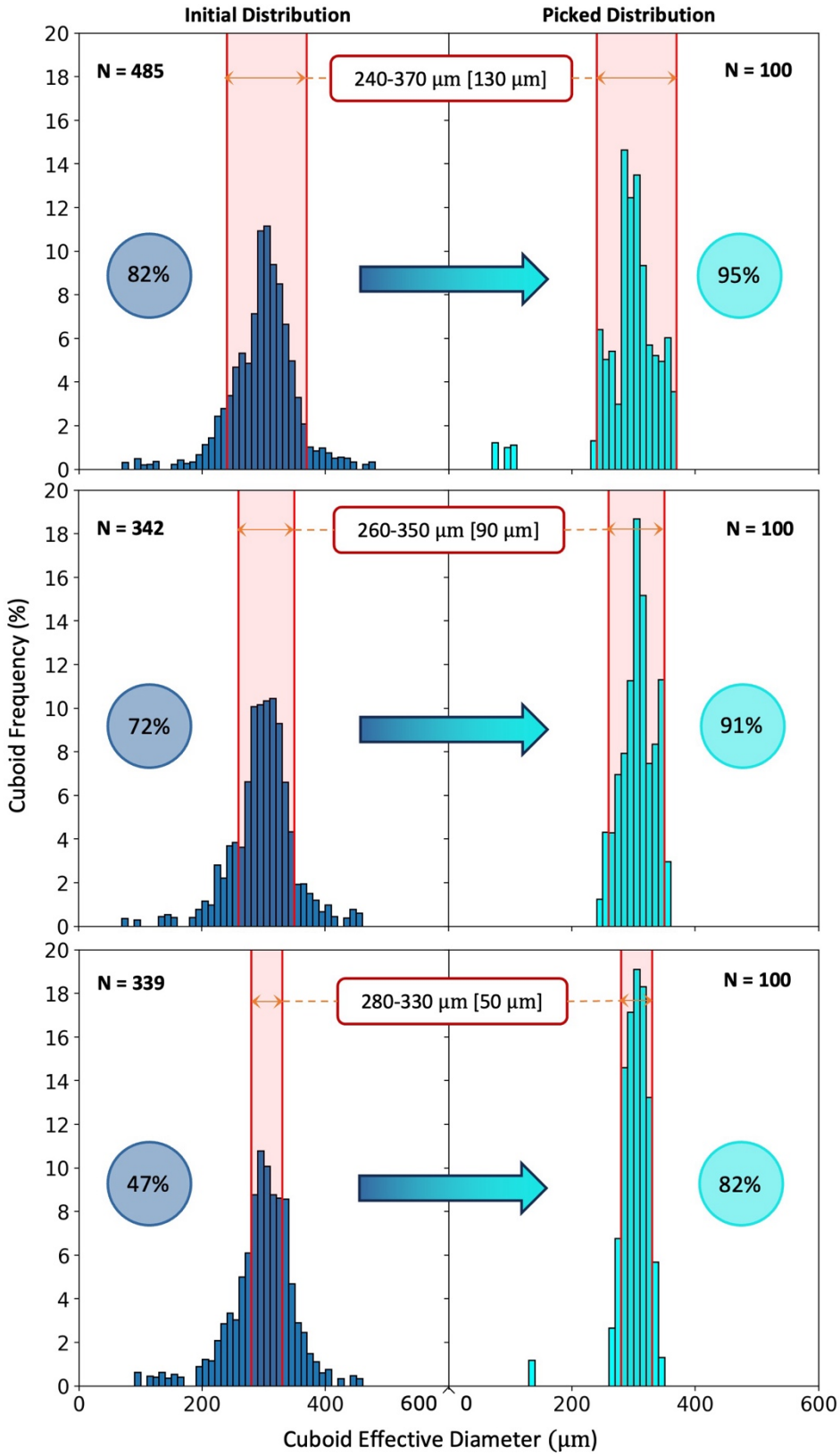

Figure 3. Robotic size sorting of cuboids. Three consecutive experiments with a decreasing picking size range from top to bottom: 130 µm, 90 µm, 50 µm respectively. The initial cuboid size distributions (before picking) are shown on the left and resulting picked cuboid size distributions are shown on the right. On the 'Picked Distribution' plots, the few < 200 µm diameter data points outside of the defined size range represent camera sensor noise and the debris in the target culture dish.

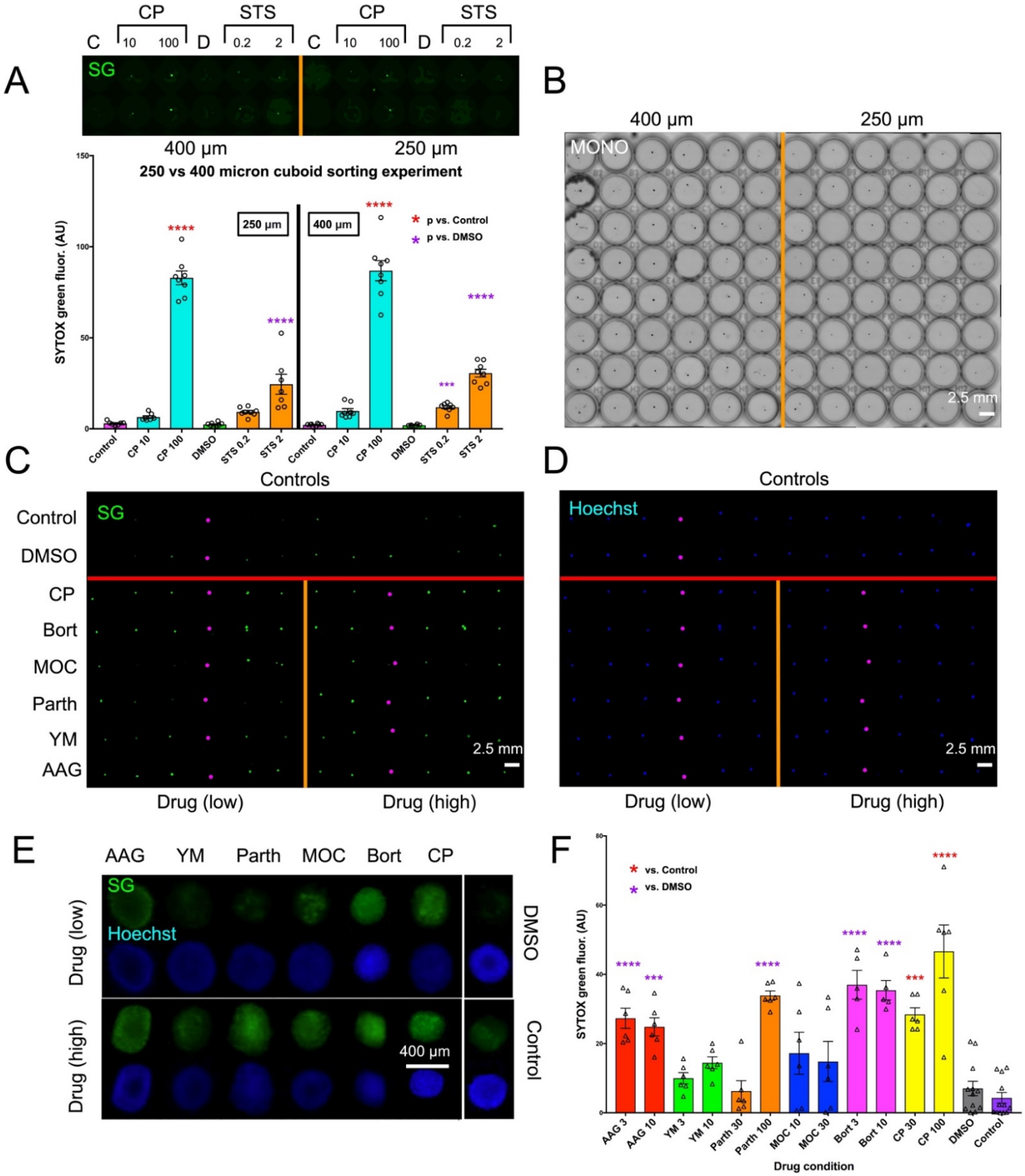

Figure 4. Fluorescent drug testing of mouse tumor cuboids in a 96-well plate. (A-B) Drug treatment of Py8119 mouse tumor cuboids. (A) Fluorescent readout of drug testing of two different sized (250 and 400 µm) cuboids in a single 96 well plate. Each cuboid is represented by an open circle. **(B)** Monochromatic image displaying the 96 well plate with the two sizes of cuboids in each half. **(C-F)** U87 xenograft tumor cuboids treated with a panel of drugs. **(C)** Fluorescent image of a 96-well plate with Sytox Green cell death fluorescent stain. **(D)** Fluorescent image of the same plate in (C) with Hoechst nuclear fluorescent stain. **(E)** Closeup of individual wells in (C) and (D), as marked.

(F) Graph of the combined fluorescent readouts of two 96-well plates. Average ± sem, with individual cuboids represented by open triangles. One-way ANOVA with Tukey post-hoc. ***p< X, ****p<Y.

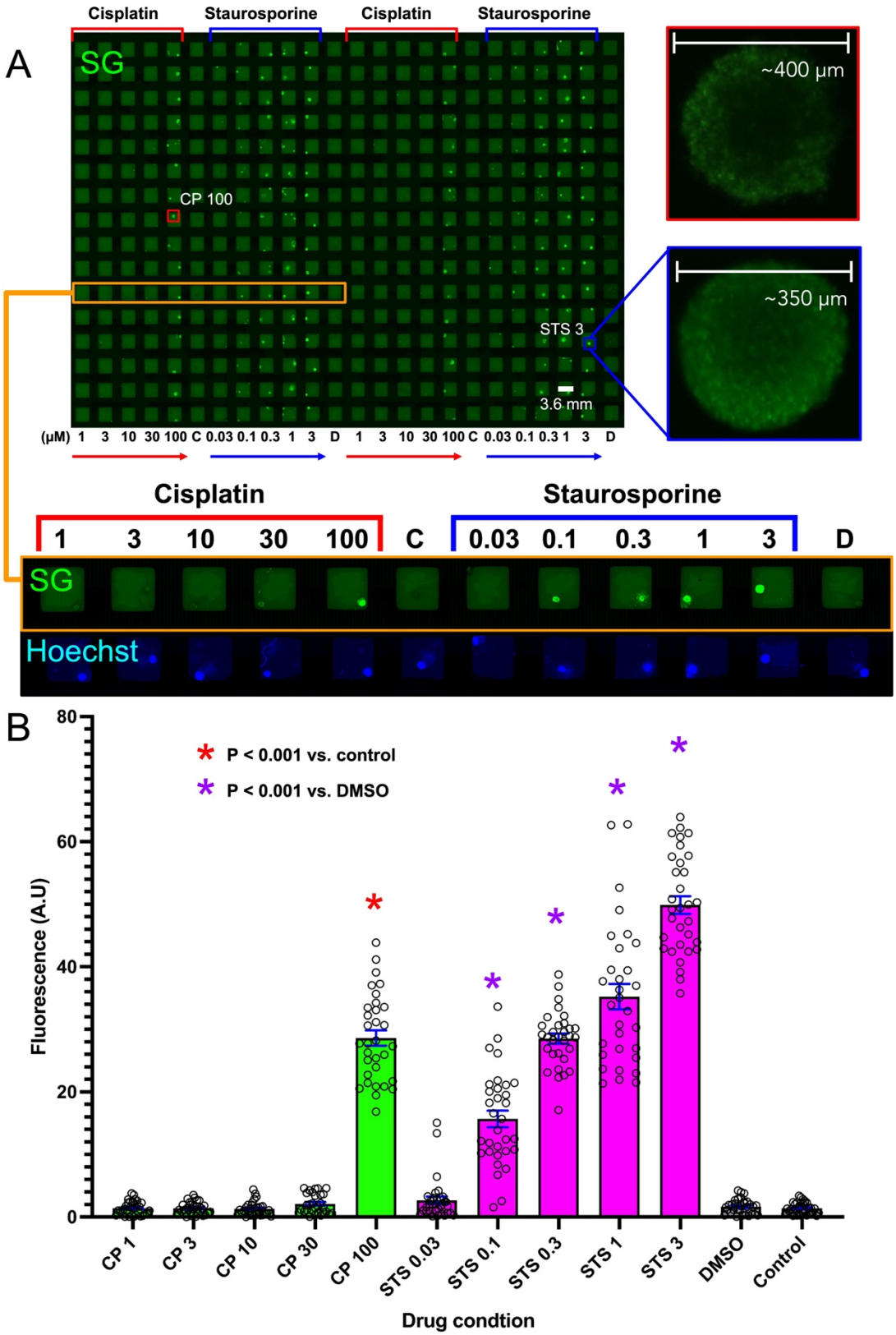

Figure 5. (A) Green channel image displaying (visually) increasing fluorescent intensity with increased drug concentration on PY8119 mouse breast cancer cuboids fluorescently stained with Sytox Green (SF) cell death stain in a 384 well plate. Close-ups below: Cisplatin (CP) and Staurosporine (STS) treatment at five different concentrations. Close-ups on the right: STS (3 µM) and CP (100 µM). **(B)** SG fluorescent readout on 384 well plate for each condition. Each cuboid is represented by an open circle. Graph of T-test, Student two-tailed T-test.

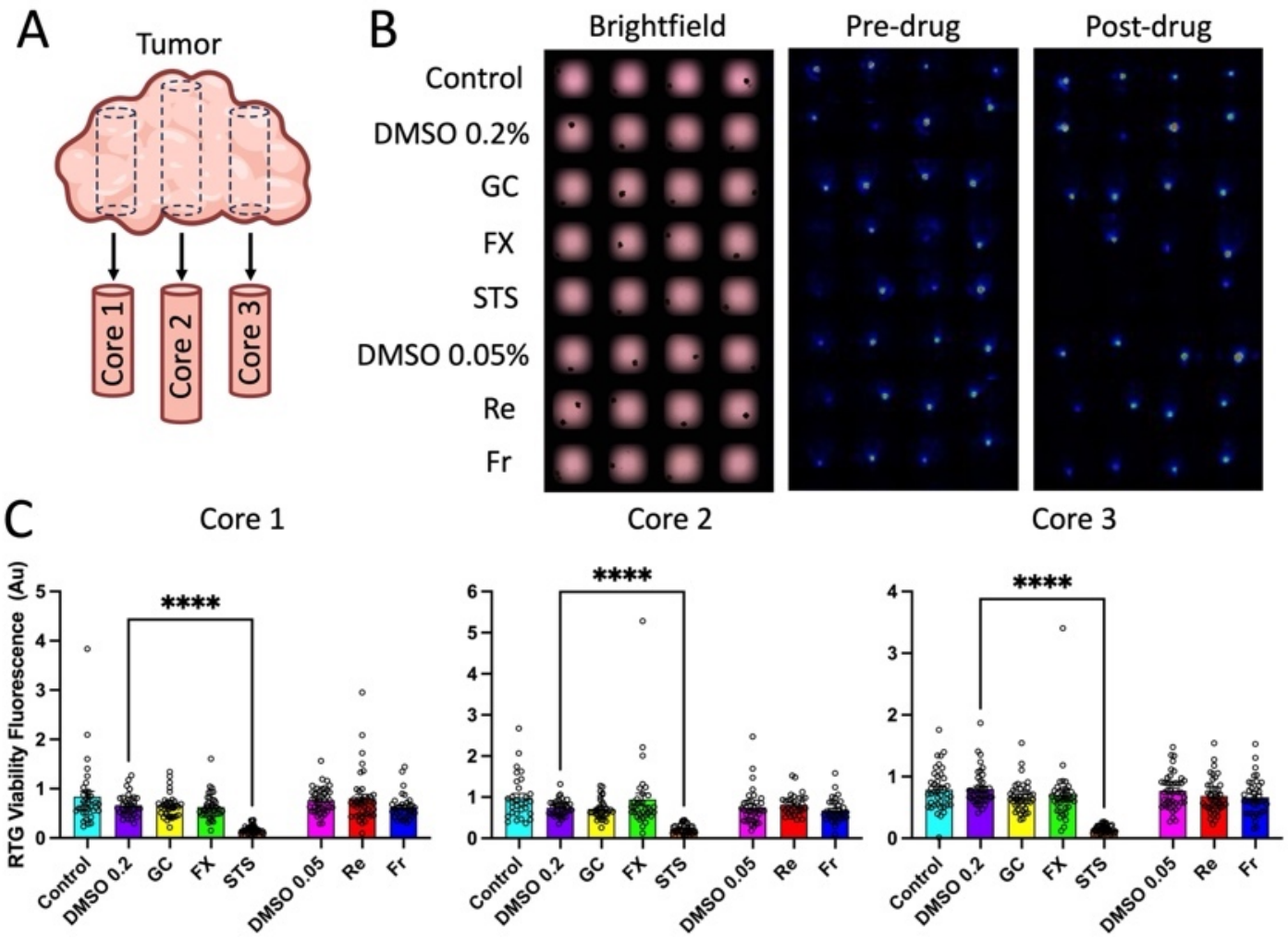

Figure 6. Drug testing on cuboids from a patient colorectal cancer liver metastasis with clinically relevant drugs. (A) Schematic of tissue preparation: three core biopsies were taken from the tumor and cuboids from each core were distributed onto separate 384-well plates. **(B)** Examples from the 384-well plate filled with cuboids from core 3. Cuboid positions within wells displayed on the leftmost brightfield photo, with each row corresponding to one condition. Baseline viability as luminescence measured with an IVIS machine is displayed in the center. Post-drug viability measured on the 6th day is displayed on the right. **(C)** Graphs of the drug response ratios (day 6 / day 1) displayed for each core/plate. Ave ± sem, with individual cuboids represented as open circles. One-way ANOVA with Tukey post-hoc. ****P< X.

REFERENCES

1. Banerjee, D., Singh, Y. P., Datta, P., Ozbolat, V., O'Donnell, A., Yeo, M. & Ozbolat, I. T. Strategies for 3D bioprinting of spheroids: A comprehensive review. *Biomaterials* **291**: 121881 (2022).
2. Leong, T. G., Randall, C. L., Benson, B. R., Zarafshar, A. M. & Gracias, D. H. Self-loading lithographically structured microcontainers: 3D patterned, mobile microwells. *Lab Chip* **8**: 1621–1624 (2008).
3. Wang, Y., Phillips, C., Xu, W., Pai, J. H., Dhopeshwarkar, R., Sims, C. E. & Allbritton, N. Micromolded arrays for separation of adherent cells. *Lab Chip* **10**: 2917–2924 (2010).
4. Moscona, A. & Moscona, H. The dissociation and aggregation of cells from organ rudiments of the early chick embryo. *J. Anat.* **86**: 287–301 (1952).
5. Gunti, S., Hoke, A. T. K., Vu, K. P. & London, N. R. Organoid and spheroid tumor models: Techniques and applications. *Cancers (Basel).* **13**: 1–18 (2021).
6. Materne, E. M., Ramme, A. P., Terrasso, A. P., Serra, M., Alves, P. M., Brito, C., Sakharov, D. A., Tonevitsky, A. G., Lauster, R. & Marx, U. A multi-organ chip co-culture of neurospheres and liver equivalents for long-term substance testing. *J. Biotechnol.* **205**: 36–46 (2015).
7. Fjellbirkeland, L., Laerum, O. D. & Bjerkvig, R. Tumour fragment spheroids from human non-small-cell lung cancer maintained in organ culture. *Virchows Arch.* **426**: 169–178 (1995).
8. Lao, Z., Kelly, C. J., Yang, X. Y., Jenkins, W. T., Toorens, E., Ganguly, T., Evans, S. M. & Koch, C. J. Improved methods to generate spheroid cultures from tumor cells, tumor cells & fibroblasts or tumor-fragments: microenvironment, microvesicles and MiRNA. *PLoS One* **10**: e0133895 (2015).
9. Aref, A. R., Huang, R. Y.-J., Yu, W., Chua, K.-N., Sun, W., Tu, T.-Y., Bai, J., Sim, W.-J., Zervantonakis, I. K., Thiery, J. P. & Kamm, R. D. Screening therapeutic EMT blocking agents in a three-dimensional microenvironment. *Integr. Biol.* **5**: 381–389 (2013).
10. Aref, A. R. *et al.* 3D microfluidic ex vivo culture of organotypic tumor spheroids to model immune checkpoint blockade. *Lab Chip* **18**: 3129–3143 (2018).
11. Jenkins, R. W. *et al.* Ex vivo profiling of PD-1 blockade using organotypic tumor spheroids. *Cancer Discov.* **8**: 196–215 (2018).
12. Ootani, A., Li, X., Sangiorgi, E., Ho, Q. T., Ueno, H., Toda, S., Sugihara, H., Fujimoto, K., Weissman, I. L., Capecchi, M. R. & Kuo, C. J. Sustained in vitro intestinal epithelial culture within a Wnt-dependent stem cell niche. *Nat. Med.* **15**: 701–706 (2009).
13. Li, X. *et al.* Oncogenic transformation of diverse gastrointestinal tissues in primary organoid culture. *Nat. Med.* **20**: 769–777 (2014).
14. Neal, J. T. *et al.* Organoid Modeling of the Tumor Immune Microenvironment. *Cell* **175**: 1972-1988.e16 (2018).
15. Kretzschmar, K. Cancer research using organoid technology. *J. Mol. Med.* **99**: 501–515 (2021).
16. Bar-Ephraim, Y. E., Kretzschmar, K. & Clevers, H. Organoids in immunological research. *Nat. Rev. Immunol.* **20**: 279–293 (2019).
17. Skylar-Scott, M. A., Uzel, S. G. M., Nam, L. L., Ahrens, J. H., Truby, R. L., Damaraju, S. & Lewis, J. A. Biomanufacturing of organ-specific tissues with high cellular density and embedded vascular channels. *Sci. Adv.* **5**: eaaw2459 (2019).
18. Sachs, N. *et al.* A Living Biobank of Breast Cancer Organoids Captures Disease Heterogeneity. *Cell* **172**: 373-386.e10 (2018).
19. Pauli, C. *et al.* Personalized in vitro and in vivo cancer models to guide precision medicine. *Cancer Discov.* **7**: 462–477 (2017).
20. Ding, S. *et al.* Patient-derived micro-organospheres enable clinical precision oncology. *Cell Stem Cell* **29**: 905-917.e6 (2022).
21. Driehuis, E., Kretzschmar, K. & Clevers, H. Establishment of patient-derived cancer organoids for drug-screening applications. *Nat. Protoc.* **15**: 3380–3409 (2020).

22. Tung, Y.-C., Hsiao, A. Y., Allen, S. G., Torisawa, Y., Ho, M. & Takayama, S. High-throughput 3D spheroid culture and drug testing using a 384 hanging drop array. *Analyst* **136**: 473–478 (2011).

23. Ganguli, A. *et al.* Three-dimensional microscale hanging drop arrays with geometric control for drug screening and live tissue imaging. *Sci. Adv.* **7**: eabc1323 (2021).

24. Horowitz, L. F., Rodriguez, A. D., Au-Yeung, A., Bishop, K. W., Barner, L. A., Mishra, G., Raman, A., Delgado, P., Liu, J. T. C., Gujral, T. S., Mehrabi, M., Yang, M., Pierce, R. H. & Folch, A. Microdissected "cuboids" for microfluidic drug testing of intact tissues. *Lab Chip* **21**: 122 (2021).

25. Astolfi, M., Peant, B., Lateef, M. A., Rousset, N., Kendall-Dupont, J., Carmona, E., Monet, F., Saad, F., Provencher, D., Mes-Masson, A. M. & Gervais, T. Micro-dissected tumor tissues on chip: an ex vivo method for drug testing and personalized therapy. *Lab Chip* **16**: 312–325 (2016).

26. Homan, K. A., Gupta, N., Kroll, K. T., Kolesky, D. B., Skylar-Scott, M., Miyoshi, T., Mau, D., Valerius, M. T., Ferrante, T., Bonventre, J. V., Lewis, J. A. & Morizane, R. Flow-enhanced vascularization and maturation of kidney organoids in vitro. *Nat. Methods* **16**: 255–262 (2019).

27. Velasco, V., Shariati, S. A. & Esfandyarpour, R. Microtechnology-based methods for organoid models. *Microsystems Nanoeng.* **6**: 76 (2020).

28. Grexa, I., Diosdi, A., Harmati, M., Kriston, A., Moshkov, N., Buzas, K., Pietiäinen, V., Koos, K. & Horvath, P. SpheroidPicker for automated 3D cell culture manipulation using deep learning. *Sci. Reports 2021 111* **11**: 1–11 (2021).

29. Kundu, P. K., Cohen, I. M. & Dowling, D. R. *Fluid mechanics*. (Academic Press, 2015).